


Article

Synthesis, Self-Assembly in Crystalline Phase and Anti-Tumor Activity of 2-(2-/4-Hydroxybenzylidene)thiazolo[3,2-*a*]pyrimidines

Artem S. Agarkov ¹, Anna A. Nefedova ¹, Elina R. Gabitova ², Alexander S. Ovsyannikov ¹ , Syumbelya K. Amerhanova ¹, Anna P. Lyubina ¹, Alexandra D. Voloshina ¹, Pavel V. Dorovatovskii ³, Igor A. Litvinov ¹, Svetlana E. Solovieva ¹ and Igor S. Antipin ^{1,*}

¹ Arbuzov Institute of Organic and Physical Chemistry, FRC Kazan Scientific Center, Russian Academy of Sciences, Arbuzova 8, 420088 Kazan, Russia

² Department of Organic and Medical Chemistry, Kazan Federal University, Kremlevskaya 18, 420008 Kazan, Russia

³ National Research Center "Kurchatov Institute", Akademika Kurchatova 1, 123182 Moscow, Russia

* Correspondence: iantipin54@yandex.ru

Abstract: A series of new thiazolo[3,2-*a*]pyrimidines different by aryl substituents in 2 and 5 positions are synthesized and characterized in solution as well as in the crystalline phase using ¹H and ¹³C NMR-, IR-spectroscopies, mass-spectrometry methods, and single crystal X-ray diffraction (SCXRD). The SCXRD study revealed the role of intermolecular H-bonding in the formation of supramolecular architectures (racemic monomers, centrosymmetric racemic dimers, or homochiral 1D chains) of obtained thiazolo[3,2-*a*]pyrimidines derivatives depending on solvents (aprotic DMSO or protic EtOH) used upon the crystallization process. Moreover, the in vitro study of cytotoxicity toward different tumor cells showed their high or moderate efficiency with moderate cytotoxicity against normal liver cells which allows to consider the obtained thiazolo[3,2-*a*]pyrimidine derivatives as promising candidates for application as antitumor agents.

Keywords: thiazolo[3,2-*a*]pyrimidines; solid-state structure; non-covalent interactions; cytotoxicity; antitumor agents; multiplex analysis of DNA markers of genotoxicity



Citation: Agarkov, A.S.; Nefedova, A.A.; Gabitova, E.R.; Ovsyannikov, A.S.; Amerhanova, S.K.; Lyubina, A.P.; Voloshina, A.D.; Dorovatovskii, P.V.; Litvinov, I.A.; Solovieva, S.E.; et al. Synthesis, Self-Assembly in Crystalline Phase and Anti-Tumor Activity of 2-(2-/4-Hydroxybenzylidene)thiazolo[3,2-*a*]pyrimidines. *Molecules* **2022**, *27*, 7747. <https://doi.org/10.3390/molecules27227747>

Academic Editors: Alexander F. Khlebnikov and Nikolai V. Rostovskii

Received: 15 October 2022

Accepted: 8 November 2022

Published: 10 November 2022

Publisher's Note: MDPI stays neutral with regard to jurisdictional claims in published maps and institutional affiliations.



Copyright: © 2022 by the authors. Licensee MDPI, Basel, Switzerland. This article is an open access article distributed under the terms and conditions of the Creative Commons Attribution (CC BY) license (<https://creativecommons.org/licenses/by/4.0/>).

1. Introduction

Heterocycles, especially those composed of different heterocyclic aromatic rings, generally possessing high biological activity represent organic compounds widely used for design of new antitumor drugs [1,2]. Among the various heterocyclic compounds in terms of antitumor activity, the thiazoles and pyrimidines derivatives are some of the most attractive precursors in medical chemistry due to their high pharmacological application in particular as anti-tuberculosis drugs, antioxidants, antimicrobial, antiviral agents, as medicaments for inflammatory disease treatment and antitumor therapy [3–8]. Nowadays, it is established that cancer of various types is a leading cause of morbidity and mortality worldwide, characterized by irregular cell growth. The number of deaths caused by cancer is still growing. According to the World Health Organization (WHO), in 2020, cancer accounts for more than 19 million new cases registered and ranks as one of the first leading cause of death in people under 70 years old [9]. For this purpose, in the past decades, the design of new heterocyclic compounds that demonstrate high antitumor activity both with low and normal cell cytotoxicity still attracts huge attention.

Recently, it was shown that due to high biological and pharmacological activities, heterocyclic compounds based on functional derivatives of 2-arylmethylidene thiazolo[3,2-*a*]pyrimidines are appealing molecules demonstrating a high potential in anticancer drug design. In particular, it was demonstrated that indole derivative of triazolopyrimidine **1** (Figure 1) exceeded the cytotoxicity efficiency of the widely used antitumor drug doxorubicin by 1.15 times in the MCF-7 breast cancer cell line [10].

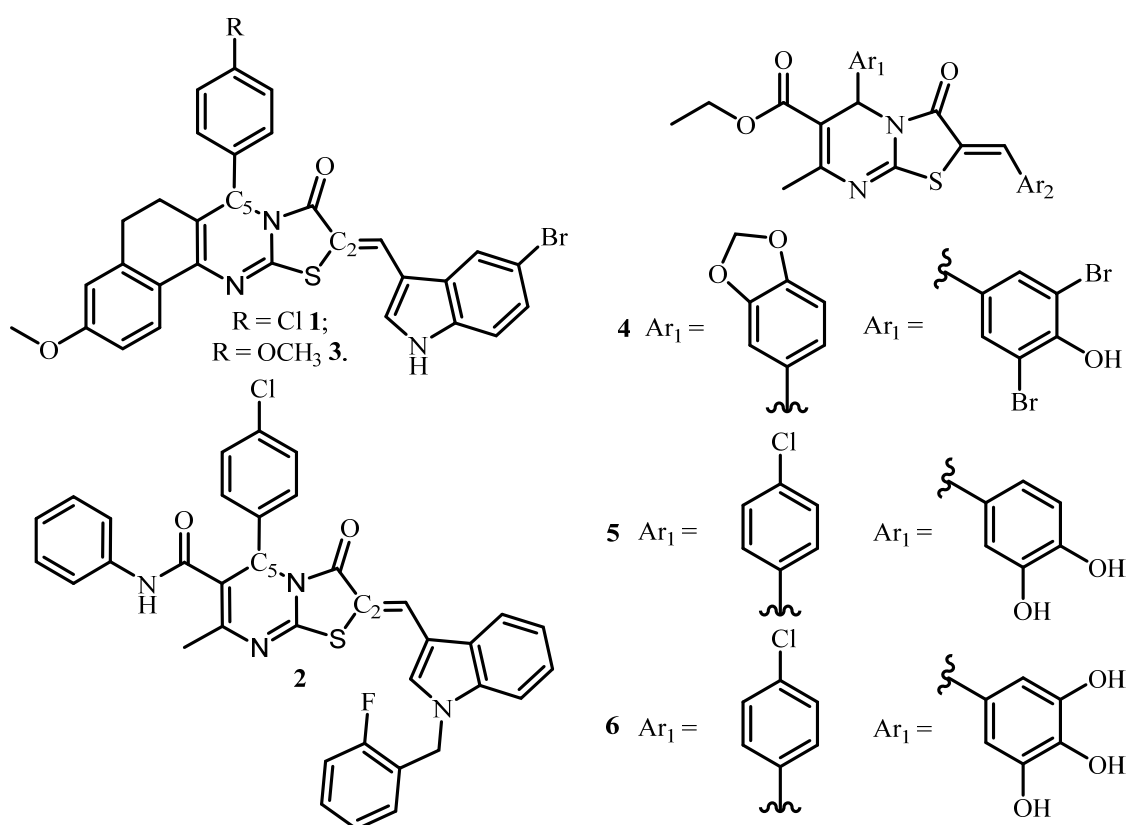


Figure 1. Thiazolo[3,2-*a*]pyrimidine compounds used as promising enzyme inhibitors and antitumor drugs.

In addition, compound **1** has demonstrated high absorption ability in the gastrointestinal tract due to optimal hydrophilicity/lipophilicity of the molecule [11]. The related compound **2** (Figure 1) has been used for the growth of Bcl-2 proteins inhibitor which leads to many types of tumor cells apoptosis [12]. Compound **3** (Figure 1) has displayed remarkable inhibiting activity of the anti-apoptotic Bcl protein with IC_{50} value of 3.4 μM , which practically corresponds to the one established for *obatoclax* drug [13]. Other similar compounds **4–6** containing thiazolo[3,2-*a*]pyrimidine fragment were found to be promising, and selective CDC25 phosphatase or casein kinase inhibitors play a key role in the regulation of the cell cycle observed in many types of cancer [14,15]. Earlier it was also reported that the triazolpyrimidine derivatives containing another molecular junction at C2 atom (dihydrazone derivatives) showed low cytotoxicity against normal and tumor cell lines [16].

Earlier, we reported on the synthesis and crystal structures of three derivatives of 2-(2-hydroxybenzylidene)thiazolo[3,2-*a*]pyrimidines containing phenyl-(**7**), 2-hydroxyphenyl-(**8**) and 4-methoxyphenyl-(**9**) substituents at the C5 carbon atom, where the conglomerate crystallization of one of the studied heterocycles (compound **8**) based on thiazolo[3,2-*a*]pyrimidine ($P2_12_12_1$ space group) into chiral 1D chains stabilized by intermolecular H-bonding is presented [17]. It should be mentioned that up to now no anti-tumor activity of the described compounds is studied.

Following this line, we synthesized three new compounds, **10–12**, bearing 2-hydroxybenzylidene substituent at the C2 carbon atom. In addition, in order to expand this series of new thiazolo[3,2-*a*]pyrimidines, the 4-hydroxybenzylidene derivatives were obtained: compound **13** (isomeric to compound **7**), compound **14** (isomeric to compound **12**), and compound **15** (isomeric to compound **10**) (Figure 2). Herein the crystal structure of the obtained compounds **9–14** is discussed below. Moreover, the study

of anti-tumor activity of a series of obtained 2-and 4-hydroxybenzylidene thiazolo[3,2-*a*]pyrimidine derivatives 7–15 is also presented.

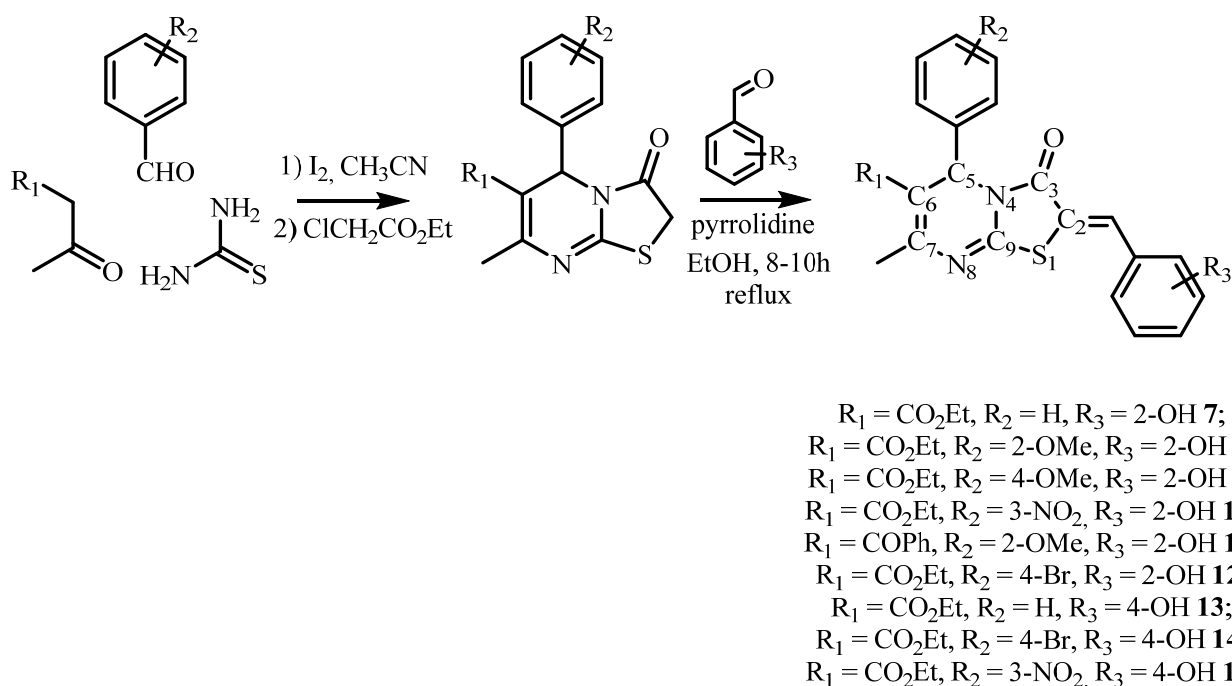


Figure 2. Synthesis of 2- and 4-(hydroxybenzylidene)thiazolo[3,2-*a*]pyrimidines 7–15.

2. Results and Discussion

All arylmethylidenethiazolopyrimidines 7–15 were synthesized following the scheme presented on Figure 2. In the first stage, a three-component Biginelli condensation involving appropriate aldehyde (benzaldehyde, 2-methoxybenzaldehyde, 4-methoxybenzaldehyde, 3-nitrobenzaldehyde, or 4-brombenzaldehyde), thiourea, and 1,3-dicarbonyl compound (acetoacetic ether or benzoylacetone) in a molar ratio 1:1.5:1 led to the preparation of 1,2,3,4-tetrahydropyrimidine-2-thions in the presence of a catalytic amount of molecular iodine (0.03 mmol) under refluxing conditions in acetonitrile as described earlier [18–22]. Then the obtained compounds were used as precursors for the synthesis of targeted 2- and 4-hydroxybenzylidene thiazolo[3,2-*a*]pyrimidine 7–15 by reaction with corresponding 2- or 4-hydroxybenzaldehydes. The desired products were obtained by filtration of the reaction mixture followed by the recrystallisation from the methanol or ethanol solution in high yields.

The structures of synthesized compounds were studied using SCXRD, whose data are in agreement with the structure of these compounds in solution (for ^1H -, ^{13}C -NMR-, IR-, and mass-spectra see Figures S1–S19). In the crystalline phase, all the obtained compounds present similar structure when all carbon atoms, except C5, as well as hetero atoms (S and N) of bicyclic thiazolo[3,2-*a*]pyrimidines fragment are located in the same plane. The asymmetric sp^3 hybridized C5 atom is found to be disposed out of thiazolo[3,2-*a*]pyrimidine plane displaying the distance of 0.126–0.273(1) Å and leading to a *sofa* conformation of six-membered pyrimidine ring (see Table S1). Interestingly, it was found out that for 12, C5 atom is found to be located in the same plane as thiazolo[3,2-*a*]pyrimidine bicyclic ring. All obtained molecules display only one C=C double bond configuration when 2- or 4-hydroxybenzylidene fragment and S atom of thiazolyl moiety are *cis*-orientated (*Z*-isomers).

The aryl substituent connected to C5 atom occupies an axial position and is disposed in the plane bisecting N4-C5-C6 angle. For 11, the intramolecular O- π bonding is observed between the *ortho* OCH₃ group of phenyl substituent disposed at C5 atom and the π -system of pyrimidine moiety ($d_{\text{O17-C3N2centroid}} = 2.731$ Å). Such type of interaction leading to stabilization of molecular conformation have been already reported recently [17,23].

Both the distances observed for C2–C9 and C9–C10 bonds as well as the dihedral angle formed between the phenol moiety of benzylidene substituent at C2 atom and thiazolo[3,2-a]pyrimidine bicyclic ring evidence the formation of a large electron-conjugated system for all compounds (see Table S1). In the crystalline phase, all studied 2-hydroxybenzylidene)thiazolo[3,2-a]pyrimidines adopt conformation when 2-OH group is found to be syn orientated with carbonyl group of thiazolyl moiety.

For ester derivatives 8–10 and 12–14, the carbonyl group positioned at C6 atom is found to be conjugated with thiazolo[3,2-a]pyrimidine system which was attested by the values of the corresponding dihedral angle (see Table S2). In contrast, the ketoaryl derivative 11 displays relatively large dihedral angle with thiazolo[3,2-a]pyrimidine fragment equal to 39°. Other characteristic bond distances and angles gathered in the Table S2 are found to be similar for all the studied compounds.

Due to presence of H-donor such as and H-acceptor atoms within the molecular structures, one may assume that the obtained thiazolo[3,2-a]pyrimidines are prone to be involved in supramolecular assemblies formation in the crystalline phase as well as in solution. It is worth noting that the propensity of such type of molecules to participate in spontaneous self-assembly upon the H-bonding may play the important role in their medical application [24,25]. Indeed, as it was established, the supramolecular organization of obtained compounds in the crystalline phase depends on the mutual orientation of H-donor/acceptor in the molecular scaffold as well as on the use of aprotic or protic solvent.

For 2-hydroxybenzylidene derivatives 9, 11, and 12, when crystallized from the ethanol solution, the formation of supramolecular racemic dimers displaying the centrosymmetric structure resulting from the intermolecular H-bonding between O11 atom of hydroxyl group and O3 atom belonging to carbonyl group of thiazolyl ring with the O...O distance range of 2.612(2)–2.797(2) Å was observed (see Figure 3, Table S3).

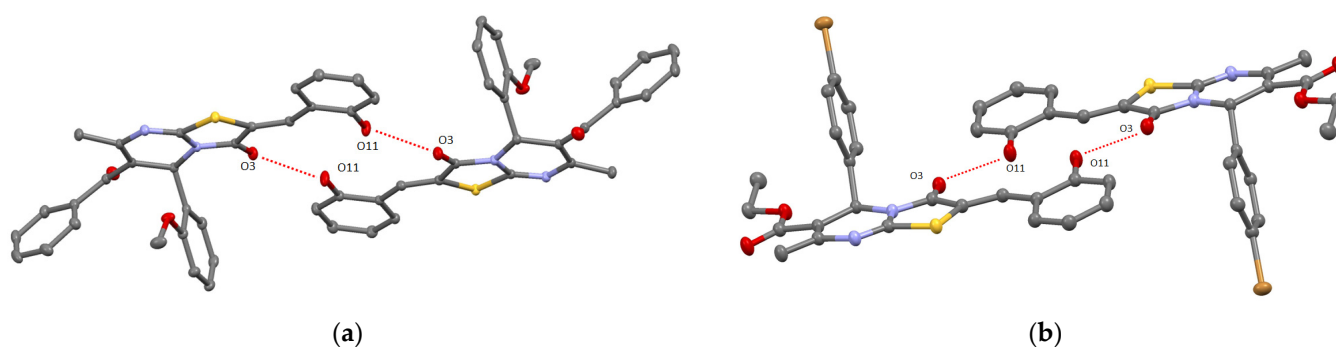


Figure 3. ORTEP-view of supramolecular dimers resulting from intermolecular H-bonding in crystals of compound 11 (a) and 12 (b). The ellipsoids are presented with 50% probability, H-atoms are omitted for clarity. H-bonding is presented by red dotted lines.

Whereas the self-assembly of dimers based on 9 led to the formation of 2D supramolecular layer due to π -stacking of thiazolo[3,2-a]pyrimidines moieties [17], and for 11, it was found out that ketophenyl C6 atom substituent displays significant π -bonding ($d_{C6\text{centroid}/C6\text{centroid}} = 3.660$ Å, dihedral angle equal to 0°) producing the chains (see Figure 4a). In addition, the obtained chains through interacting with each other through intermolecular pyrimidine-(2-hydroxy)phenyl π -bonding ($d_{C3N2\text{centroid}/C6\text{centroid}} = 3.670$ Å, dihedral angle equal to 0°) also results in 2D supramolecular layers running along (022) crystallographic plane.

The changing of 2-or 4-methoxyphenyl substituent at C6 atom in 11 and 9 by 4-bromophenyl fragment in 12 surprisingly led to the formation of 1D chain composed of H-bonded supramolecular dimers stacked through CH/ π -bonding of C23 atom of ester group with bromophenyl moiety of adjacent molecules of 12 ($d_{C23-C6\text{centroid}} = 3.505$ Å) (see Figure 4b).

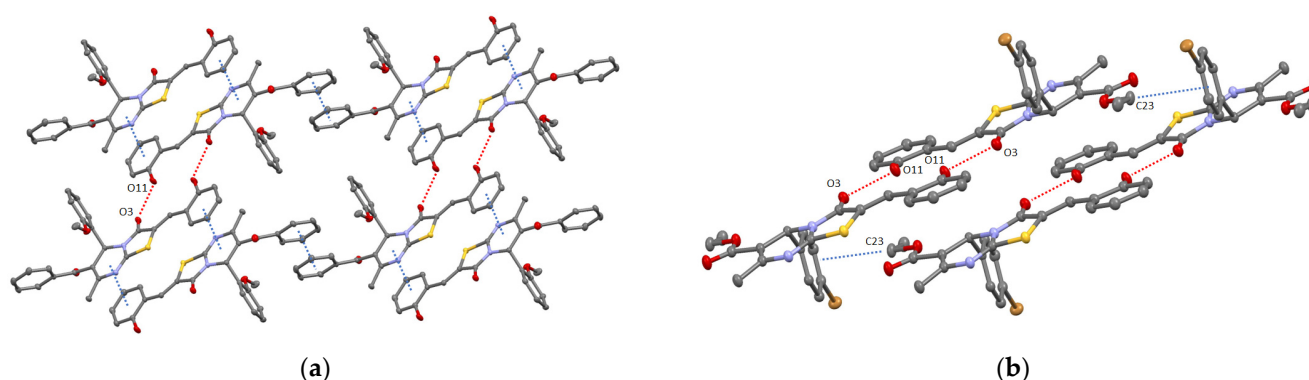


Figure 4. ORTEP view of crystal packing of **11** (a) and **12** (b) showing 2D layer and 1D chain formation resulting from both the intermolecular H-bonding and/or π - π /CH- π interactions (red and blue dotted lines, respectively). The ellipsoids are presented with 50% probability, H-atoms are omitted for clarity.

In crystal, all supramolecular dimers **9**, **11**, and **12** demonstrate the parallel crystal packing. No solvent molecules were found in the unit cell of **9**, **11**, and **12**.

Compounds **9** and **12** were also crystallized from DMSO solution. The SCXRD revealed the destroying of the H-bonded dimer assembly caused by the formation of solvate complexes **9-DMSO** [17] and **12-DMSO** in which solvent molecule was H-bonded via O30 atom with O11 atom of hydroxyl group of heterocycle (see Table S3, Figure 5). This is a remarkable example of the control on the self-assembly process using aprotic solvent displaying high H-accepting ability. In crystal of **12-DMSO**, the solvate complexes are stacked into the chains due to weak π - π and Br/ π bonding (see Figure S19). It should be noted that in **9-DMSO** and **12-DMSO**, molecules **9** and **12** adopt syn-orientation of carbonyl and hydroxyl groups and present flattened structure which has been already observed in the case of supramolecular H-bonded dimers **9**, **11**, and **12** (see Figure 3).

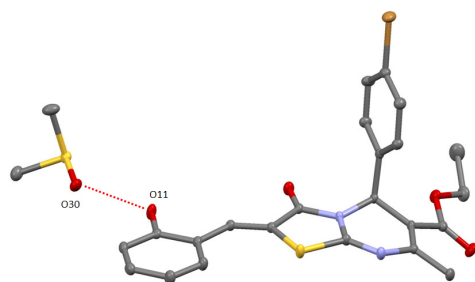


Figure 5. ORTEP-view of solvate complex **12-DMSO**. The ellipsoids are presented with 50% probability, H-atoms are omitted for clarity. H-bonding is presented by red dotted lines.

The use of methanol as a solvent upon the crystallization of compound **10** led to the generation of another solvate complex **10-MeOH** presenting the formation of zigzag homochiral chains. The MeOH molecules in **10-MeOH** forming the H-bonds with N8 atom of pyrimidine fragment and O11 atom of 2-hydroxybenzylidene moiety act as bridges connecting two adjacent thiazolo[3,2-a]pyrimidine molecules (see Table S3, Figure 6a). Within the chains, heterocyclic molecules display coplanar orientation. A similar connectivity pattern has been already observed earlier for **7-EtOH** [17], but **10-MeOH** displays a OON angle between the hydrogen bonds equal to $106.37(5)^\circ$, which is less compared to the one observed for **7-EtOH** (157.90°). In crystal, the 1D chains are stacked parallelly forming 2D layers along (002) crystallographic plane due to π - π interaction between the thiazolyl groups ($d_{C2-C3N_{\text{centroid}}} = 3.494 \text{ \AA}$, dihedral angle equal to 0°) and 2-hydroxybenzylidene moieties ($d_{C9-C6_{\text{centroid}}} = 3.561 \text{ \AA}$, dihedral angle equal to 0°) (Figure 6b).

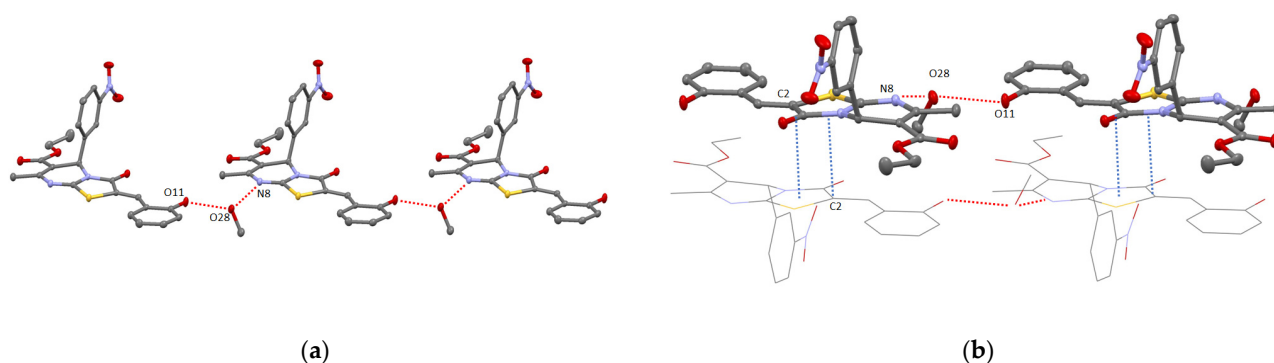


Figure 6. ORTEP view of supramolecular 1D chains resulting from intermolecular H-bonding in the crystals of compound **10-MeOH** (a) and π -stacking involving the thiazolyl groups (b). The ellipsoids are presented with 50% probability, H-atoms are omitted for clarity. H-bonding and π -stacking are presented by red and blue dotted lines, respectively.

In order to study the influence of hydroxyl group position within the structure of benzylidene substituent, the crystals of new 4-hydroxybenzylidenethiazolo[3,2-a]pyrimidines **13** and **14** were obtained by slow evaporation of their EtOH or DMSO solutions and analysis using SCXRD (see Experimental part). It was established that a self-assembly of **13** and **14** in the absence of strong H-acceptors results in 1D infinite zigzag homochiral chains formation involving the intermolecular H-bonding between O13 atom of 4-hydroxyl group acting as H-donor with N8 atom of pyrimidine fragment behaving as H-acceptor (see Table S3, Figure 7). For **13**, a weak chalcogen bonding between the O atom from hydroxyl group and S-atom from thiazolyl ring is also observed ($d_{\text{O13A-S1B}} = 3.301(6)$ Å).

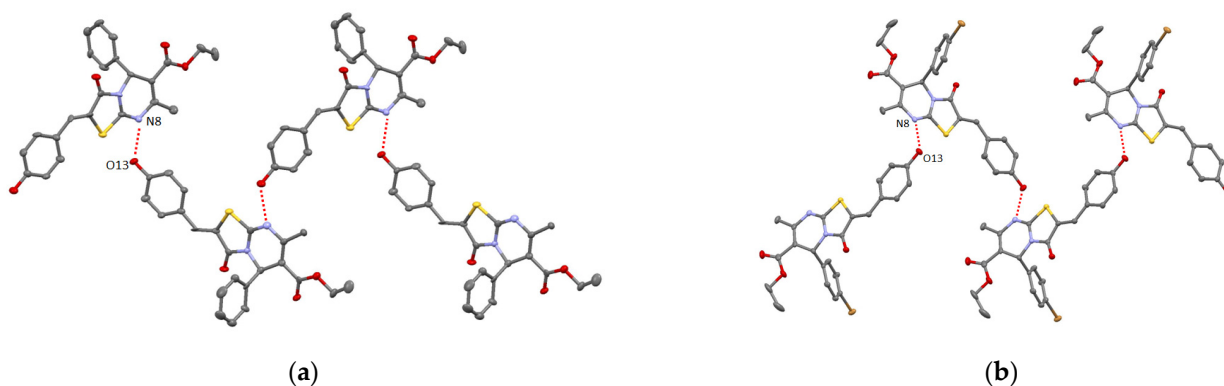


Figure 7. ORTEP view of supramolecular 1D homochiral chains formation of **13** (a) and **14** (b). The ellipsoids are presented with 50% probability, H-atoms are omitted for clarity.

Although **13** and **14** demonstrate the similar supramolecular motif of zigzag chain and dihedral angle between adjacent heterocyclic molecules within the chain structure equal to 65° , they are different by their crystal packing. In crystal of **13**, the obtained chains are stacked without any specific intermolecular interactions. For **14**, in contrast to **13**, the formation of 3D supramolecular network is observed resulting from the π -stacking thiazolyl and 4-hydroxybenzylidene moieties of heterocyclic molecules belonging to neighboring chains ($d_{\text{C10-C3NS}} = 3.566$ Å, dihedral angle equal to 0°) as well as the intermolecular O- π bonding involving O22 atom and thiazolyl moieties ($d_{\text{O22-C3NScentroid}} = 3.098$ Å, $\varphi = 142.27^\circ$) (see Figure 8 and Figure S20).

As for **9**, **11**, and **12**, the use of DMSO as a solvent upon crystallization afforded the formation of solvate **14-DMSO** in the crystalline phase where DMSO was found to be H-bonded with O11 atom belonging to hydroxyl group of **14**. It is worth noting that involvement of DMSO in H-bonding with heterocyclic compound led again to the destruction of the infinite polymeric chains (Figure 9) observed for **13** and **14** when crystallized from

ethanol solution. As for **12-DMSO**, **14-DMSO** molecules are stacked in the crystalline phase into the chains resulting from the halogen- π bonding displaying a shorter distance between Br atom and thiazolyl group equal to $d_{\text{Br1-C2}} = 3.226(1) \text{ \AA}$ (see Figure S21) with respect to **12-DMSO** (see Figure S19).

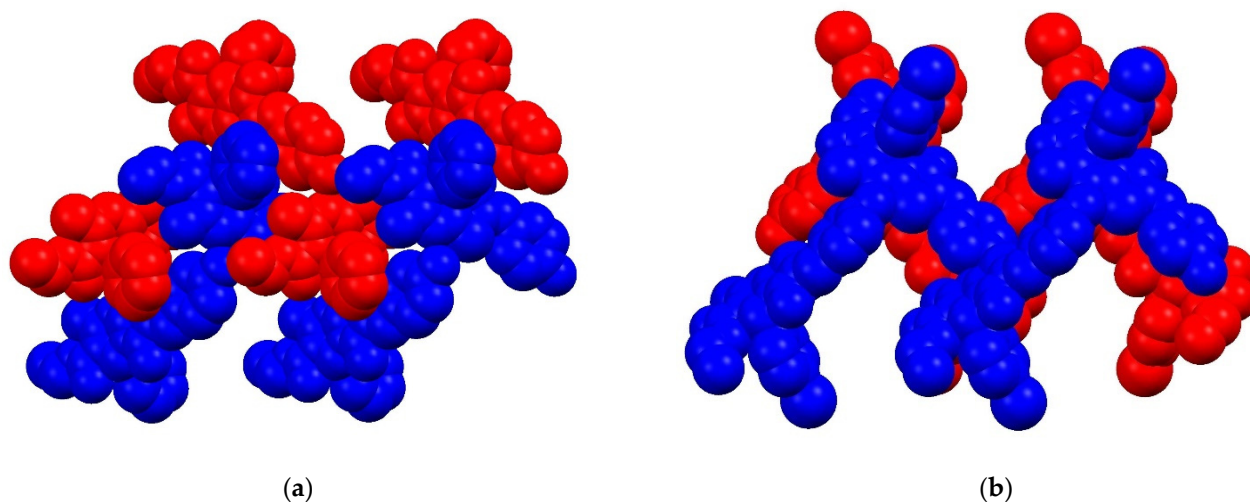


Figure 8. A portion of crystal packing of R- and S-homochiral chains (colored in blue and red, respectively) for **13** (a) and **14** (b).

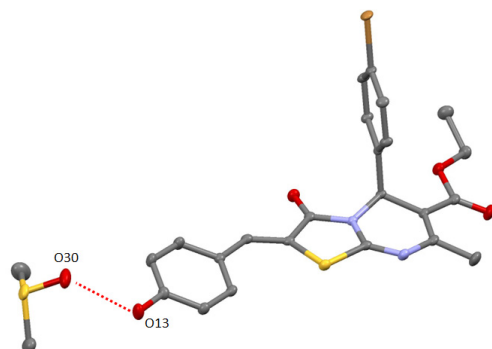


Figure 9. Crystal structure of solvate complex **14-DMSO**.

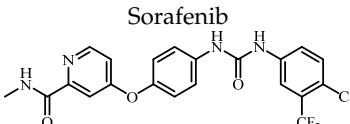
The most important stage in the investigation of new chemical compounds able to be used as potential drugs is the study of their cytotoxic properties. All prepared compounds were tested for their cytotoxicity against cancer and normal cell lines (Table 1). Data on cytotoxic activity are represented by IC_{50} values (the concentration which causes the death of 50% of cells in the experimental population).

The tested compounds showed high and moderate activity against a number of cancer lines of various genesis and demonstrated moderate cytotoxicity against normal liver cells. The most significant results were shown in the case of cell lines of cervical carcinoma (M-HeLa) and human duodenal adenocarcinoma (HuTu80). Their cytotoxic effect was manifested at the level of the comparison drug sorafenib, and for **7**, with respect to M-HeLa, it was found to be doubly increased compared to the known antitumor drug.

The selectivity of compounds against cancer cells is an important criterion for assessing the cytotoxic effect. For this purpose, the selectivity index (SI) was calculated as a ratio between the IC_{50} value for normal cells and the IC_{50} value for cancer cells. The selectivity index values for the tested compounds are shown in Table 2. It can be seen that the highest selectivity against the cancer lines M-HeLa and HuTu 80 was demonstrated by compound **7**, whose SI value was 6.0 and 7.5, respectively. Generally, the compounds with $\text{SI} \geq 3$ [26] are considered selective. According to these data, compound **7** can be considered selective

toward the M-HeLa and HuTu 80 cell lines. It was worth noting that the reference drug sorafenib showed significantly lower selectivity with respect to 7.

Table 1. Cytotoxic effects (IC₅₀, μM) of test-compounds.

Test Compounds	IC ₅₀ (μM)				
	Cancer Cell Lines				Normal Cell Lines
	M-HeLa ^a	MCF-7 ^b	PC3 ^c	HuTu 80 ^d	Chang Liver (HeLa) ^e
7	11.9 ± 0.9	43.7 ± 3.5	77.6 ± 6.7	10.2 ± 0.8	75.0 ± 5.7
8	90 ± 8.3	93.3 ± 8.2	93.7 ± 8.5	85.9 ± 8.0	56.4 ± 4.5
9	20.6 ± 1.7	32.1 ± 2.5	23.3 ± 1.9	26.8 ± 2.1	22.7 ± 1.8
10	55.0 ± 4.4	56.0 ± 4.5	56.0 ± 4.4	60 ± 4.7	88.0 ± 7.0
11	56.4 ± 4.5	81.0 ± 7.4	54.0 ± 4.3	39.0 ± 3.1	64.0 ± 5.1
12	18.8 ± 1.5	22.3 ± 1.4	28.1 ± 2.2	23.7 ± 1.8	78.2 ± 6.2
13	70.0 ± 5.5	>100	54.0 ± 4.3	43.3 ± 3.5	86.1 ± 6.8
14	31.0 ± 2.4	53.3 ± 4.2	49.3 ± 3.9	32.1 ± 2.5	53.2 ± 4.2
15	>100	>100	70.0 ± 5.5	74.5 ± 5.7	91.4 ± 7.2
 Sorafenib	25.0 ± 1.8	27.5 ± 2.2	12.7 ± 1.1	13.0 ± 1.2	21.7 ± 1.7

The experiments were performed in triplicate. Results are expressed as the mean ± standard deviation (SD); ^a M-HeLa clone 11—epithelioid carcinoma of the cervix, subline HeLa, clone M-HeLa; ^b MCF-7 is an epithelial-like cell line derived from invasive human mammary duct adenocarcinoma; ^c PC3—prostate adenocarcinoma cell line from ATCC (Collection of American-type cells, USA); ^d HuTu 80—human duodenal adenocarcinoma from the collection of the Institute of Cytology of the Russian Academy of Sciences (St. Petersburg); ^e Chang liver (HeLa derivative)—human liver cells from the collection of the Research Institute of Virology of the Russian Academy of Medical Sciences (Moscow).

Table 2. Cytotoxic effects (μM) and selectivity index values (SI) of lead compounds.

Test Compounds	Normal Cell Lines									
	M-HeLa ^a		MCF-7 ^b		PC3 ^c		HuTu 80 ^d		Chang Liver (HeLa) ^e	
	IC ₅₀	SI	IC ₅₀	SI	IC ₅₀	SI	IC ₅₀	SI	IC ₅₀	SI
7	11.9 ± 0.9	6.3	43.7 ± 3.5	1.7	77.6 ± 6.7	ns	10.0 ± 0.8	7.5	75.0 ± 5.7	
9	20.6 ± 1.7	1.1	32.1 ± 2.5	ns	23.3 ± 1.9	ns	26.8 ± 2.1	ns	22.7 ± 1.8	
10	55.0 ± 4.4	1.6	56.0 ± 4.5	1.6	56.0 ± 4.4	1.6	14.6 ± 0.3	6.0	88.0 ± 7.0	
12	18.8 ± 1.5	4.2	52.7 ± 4.2	1.5	28.1 ± 2.2	2.8	23.7 ± 1.8	3.3	78.2 ± 6.2	
Sorafenib	25.0 ± 1.8	ns	27.5 ± 2.2	ns	27.5 ± 2.2	ns	13.0 ± 1.2	1.7	21.7 ± 1.7	

The experiments were performed in triplicate. Results are expressed as the mean ± standard deviation (SD); ns—no selectivity; ^a M-HeLa clone 11—epithelioid carcinoma of the cervix, subline HeLa, clone M-HeLa; ^b MCF-7 is an epithelial-like cell line derived from invasive human mammary duct adenocarcinoma; ^c PC3—prostate adenocarcinoma cell line from ATCC (Collection of American-type cells, USA); ^d HuTu 80—human duodenal adenocarcinoma from the collection of the Institute of Cytology of the Russian Academy of Sciences (St. Petersburg); ^e Chang liver (HeLa derivative)—human liver cells from the collection of the Research Institute of Virology of the Russian Academy of Medical Sciences (Moscow).

Apoptosis is one of the most important mechanisms used for screening new anticancer agents. Apoptotic effects in M-HeLa cells were evaluated by flow cytometry using annexin V kits that can bind phosphatidylethylserine. Phosphatidylserine is contained in minimal amounts on the membrane surface of healthy cells. Therefore, the interaction of annexin V with these cells is insignificant. During apoptosis, phosphatidylserine molecules can interact with the protein. This interaction leads to an increase in the fluorescence intensity of apoptotic cells which is detected by a flow cytometer. Apoptosis-inducing effect was evaluated using the leading compound 7 at concentrations of IC₅₀/2 and IC₅₀ on the M-HeLa cell line (see Figure 10). After 24-h incubation in the presence of 7, dose-

dependent apoptosis was observed in M-HeLa cells. Moreover, the observed effects were more active at the late stage of apoptosis.

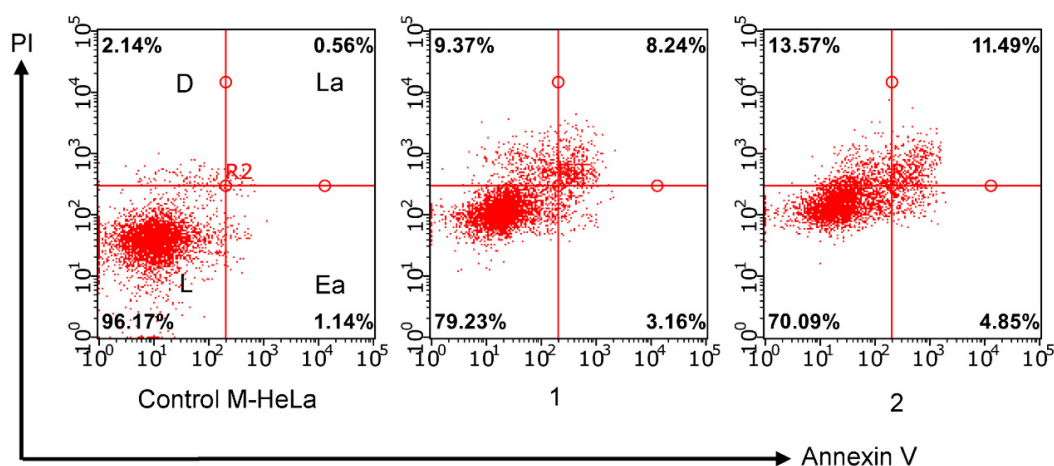


Figure 10. Induction of apoptosis in M-HeLa cells incubated with compound 7. 1—at concentration $IC_{50}/2$ (6 μ M); 2—at concentration IC_{50} (12 μ M); L—living cells; D—dead cells; Ea—early apoptotic cells; La—late apoptotic cells.

Evaluation of the mitochondria functions of the cell is another universal sign of apoptosis characteristic of eukaryotes [27]. With mitochondrial dysfunction, proapoptotic factors are released into the cytoplasm—cytochrome C, AIF, Smac/DIABLO, endonuclease G, as well as proforma caspases 2, 3, and 9—inducing cascade of caspases [28]. The output of these protein factors can be realized both by breaking mitochondrial membranes and by activating specific channels in the outer membrane of mitochondria. The events described above are usually accompanied by a change in the permeability of the inner membrane of mitochondria for H^+ protons, which leads to a change in the membrane potential of mitochondria ($\Delta\Psi_m$). Methods for studying the membrane potential of mitochondria using flow cytometry are based on the use of cationic lipophilic dyes, which in the literature are called “mitochondrial probes”. The principle of operation of these dyes is very simple—lipophilic probes spontaneously penetrate bilipid membranes (the surface membrane of the cell, as well as the outer and inner membranes of mitochondria) and accumulate in areas with a high pH value, that is, under the inner membrane of mitochondria. This effect results in a change of the intensity of cell fluorescence observed during the analysis on a flow cytometer. In this study, the fluorescent dye JC-10 from the Mitochondria Membrane Potential Kit was used to assess the change in $\Delta\Psi_m$ under the action of compound 7 at concentrations of $IC_{50}/2$ and IC_{50} on the M-HeLa cell line. JC-10 accumulates in the mitochondrial matrix and forms aggregates (J-aggregates) with red fluorescence in normal cells evidencing a high potential of the mitochondrial membrane. The mitochondrial membrane potential was found reduced in apoptotic cells which can be related with JC-10 starting to diffuse from the mitochondria and turning into a monomeric form (J-monomer) exhibiting green fluorescence. A decrease in the mitochondrial membrane potential of M-HeLa cells was observed after 24 h of treatment with the leading compound 7. The effect becomes more significant with an increase in the concentrations of the tested compounds up to IC_{50} (see Figures 11 and 12). The obtained results confirm that the mechanism of cytotoxic action of 7 can be associated with the induction of apoptosis along the internal mitochondrial pathway.

An increase in the production of reactive oxygen species (ROS) by compounds also characterizes the development of apoptosis along the mitochondrial pathway. Mitochondria are both a potential source and target of ROS. An increase in ROS production leads to the disruption of mitochondrial functions and, subsequently, to irreversible damage to cells. In this regard, the effect of the leader compound 7 at $IC_{50}/2$ and IC_{50} concentrations on ROS production in M-HeLa cells was investigated using flow cytometry analysis and CellROX[®]

Deep Red flow cytometry kit. The data presented in Figure 13 show a significant increase in the fluorescence intensity of CellROX[®] Deep Red compared to the control (unpainted cells). This indicates an increase in ROS production in the presence of the tested compound 7.

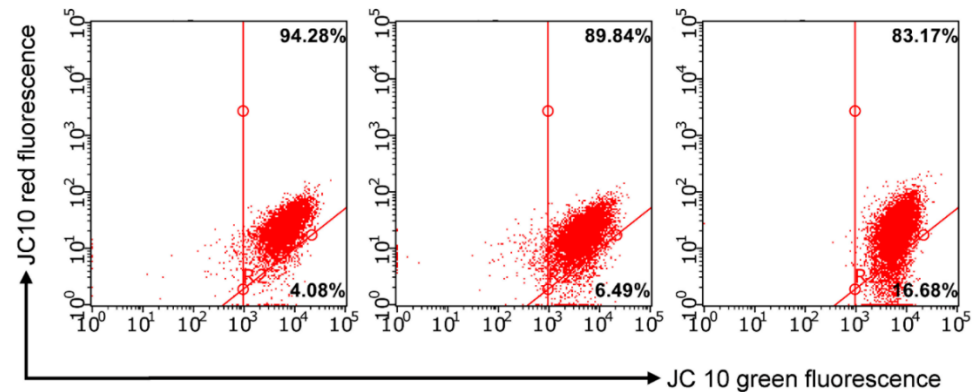


Figure 11. Effects on the mitochondrial membrane potential by 7 in M-HeLa cells. 1—at concentration IC₅₀/2 (6 μM); 2—at concentration IC₅₀ (12 μM).

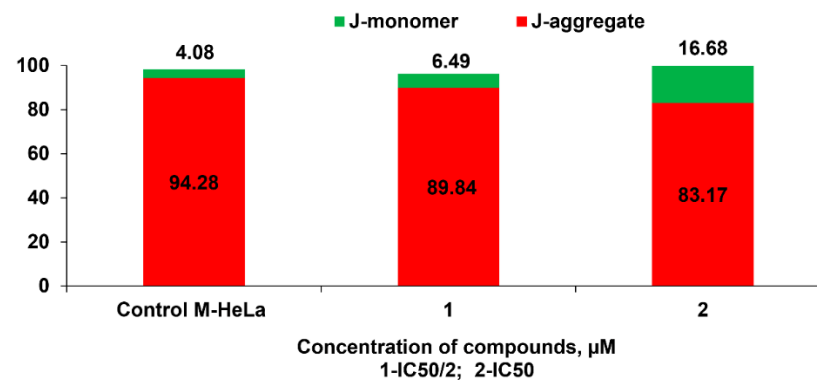


Figure 12. Quantitative determination of % M-HeLa cells with red and green aggregates. 1—at concentration IC₅₀/2 (6 μM); 2—at concentration IC₅₀ (12 μM).

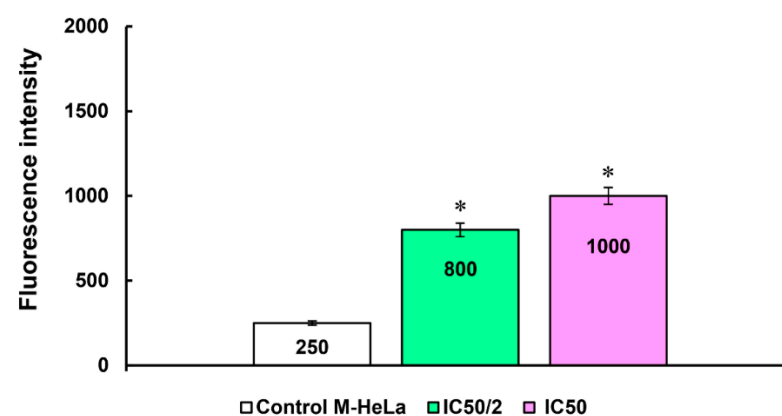


Figure 13. Induction of ROS production by compound 7. 1—at concentration IC₅₀/2 (6 μM); 2—at concentration IC₅₀ (12 μM). * Values indicate $p < 0.05$.

The effect of cytotoxic agents in general may be associated with a violation of the passage of eukaryotic cells phases of the cell cycle. This synchronizes and slows down the proliferation of a population of rapidly multiplying cells. The analysis of the cell cycle by quantifying the DNA content in the cell is a reliable research method that allows us to assess at which phase the cell cycle was stopped. This method allows us to study the phases of the cell cycle: the distribution of cells by G1/G0-, S-, and G2/M-phases of the cell

cycle is estimated by determining the relative DNA content in cells using DNA-binding fluorescent dyes such as PI (propidium iodide), 7-AAD (7-aminoactinomycin), DAPI (4',6'-diamidino-2-phenylindole (DAPI)), Hoechst, SybrGreen, etc. Anomalies of the cell cycle detected on the histogram of DNA content frequencies are often observed after various types of cell damage, especially after exposing to chemical agents. In this work, cell cycle studies were carried out using the example of the leader compound 7 at concentrations of $IC_{50}/2$ and IC_{50} on the M-HeLa cell line using the fluorescent dye propidium iodide (PI). The fluorescence intensity of the stain cells correlated with the amount of DNA contained in them. The results of the cell cycle analysis after treatment with compound 7 for 24 h at concentrations of $IC_{50}/2$ and IC_{50} on the M-HeLa cell line showed a significant delay of cells in the G0/G1 phase compared with the reference sample (Figure 14).

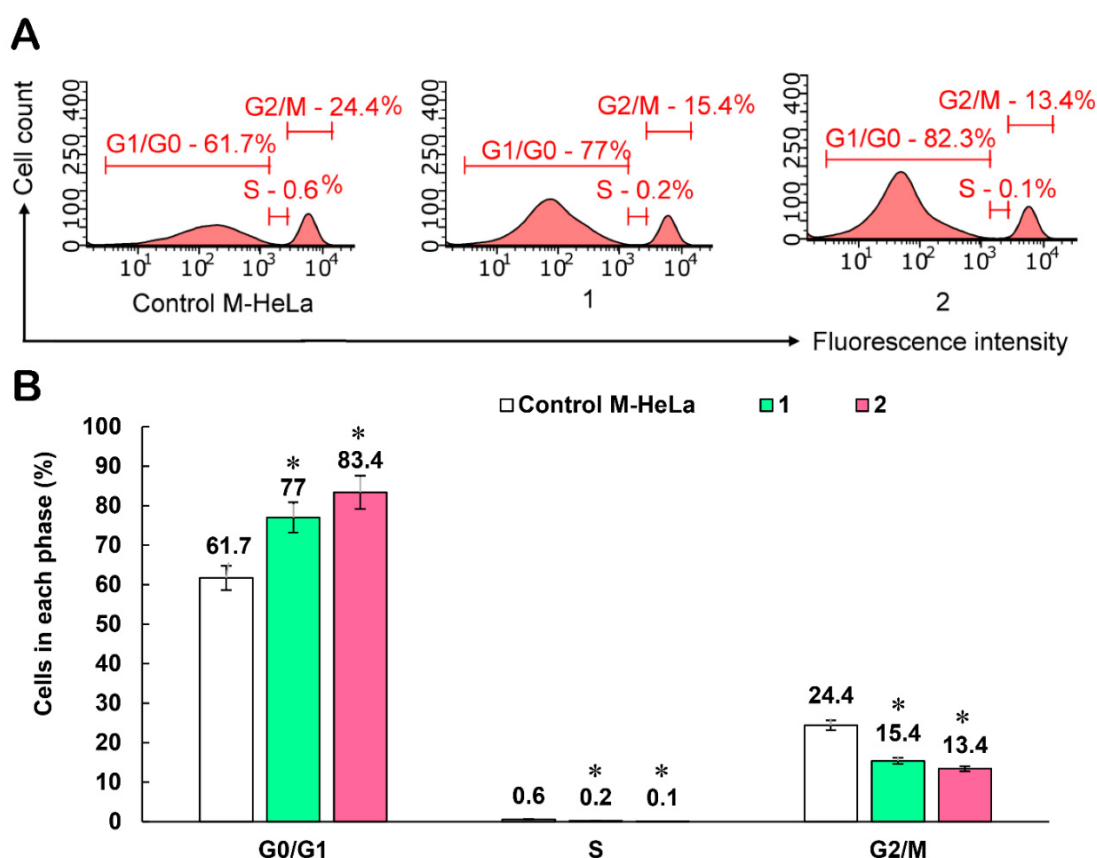


Figure 14. Effect of compound 7 on M-HeLa cell cycle arrest. 1—at concentration $IC_{50}/2$ (6 μ M); 2—at concentration IC_{50} (12 μ M); (A) cell distribution histograms. (B) Percentage of cells in the G0/G1, S, and G2/M phases (data are presented as mean \pm SD of three independent experiments). * Values indicate $p < 0.05$.

The processes of DNA damage and repair constantly occur in living cells. They can be caused by natural causes as a result of cellular respiration and metabolism or exposure to various chemical agents. Restoration of DNA damage is necessary for the normal functioning of cells and their preservation in a healthy state. Many proteins are involved in the processes of detecting and repairing DNA damage, among which groups of sensor proteins, mediators, converters, and effectors should be noted. Sensory proteins, such as Rad9, Rad1, and Hus1, accumulate at the site of DNA damage and provide phosphorylation of checkpoint proteins, which is influenced by intracellular kinases—ATM (ataxia-telangiectasia mutated) and ATR (ataxia-telangiectasia). Activation of mediator proteins such as H2AX, BRCA1, and SMC1, leads to stable protein–protein interaction, which facilitate the transmission of signals to intracellular kinases and at the same time activate checkpoint kinases. The kinases of the control points Chk1 and Chk2 are necessary

to stop the cell cycle of the main control points, G1/S and G2/M, on which the integrity of the genome is checked. Vnutyuclear kinases ATR and ATM play an important role in the delay of the cell cycle in response to DNA damage. Intermediary proteins, such as Mre11 and MDC1, acquire post-translational modifications that are created by means of detector proteins. The intermediary proteins modified in this way then amplify the signal and transmit it to effector proteins such as Chk2, MDM2, and p53. The tumor suppressor protein p53 plays a crucial role in the cell cycle arrest or apoptosis after various stresses, including chemical damage to DNA. The main target of p53 is p21 (a cyclin-dependent kinase inhibitor), which causes the cell cycle to stop at the G1/G0 stage. The coordinated functioning of the protein groups described above and some others causes the cell cycle to stop, which makes possible to control DNA damage [29].

Classical methods of assessing genotoxicity reveal mutations associated with increased or loss of function, but are not informative enough in studying the molecular mechanisms of DNA damage. The MILLIPLEX[®] MAP 7-plex DNA Damage/Genotoxicity Magnetic Bead kit allows to detect the expression and phosphorylation of a number of proteins involved in DNA damage, providing a faster and more accurate assessment of the state of the cell after exposure to genotoxic compounds. The 7-plex DNA Damage/Genotoxicity Magnetic Bead Kit is used to detect changes in phosphorylated Chk1 (Ser345), Chk2 (Thr68), H2AX (Ser139) and p53 (Ser15), as well as total protein levels of ATR, MDM2, and p21 in cellular lysates using the Luminex[®] system. Figure 15 shows the data of multiplex analysis performed using the 7-plex DNA Damage/Genotoxicity Magnetic Bead Kit. The obtained results characterize the effect of the leading compound 7 on the DNA of M-HeLa cells at concentrations of IC₅₀/2 and IC₅₀. It is shown that the values of the average fluorescence intensity of the markers Chk1, Chk2, H2AX, MDM2, p53, and p21 significantly increase with increasing concentration compared to the control untreated compound 7 samples. The fluorescence intensity of OTR markers also increases relative to the reference sample. A high concentration of p21 protein may indicate the arrest of the M-HeLa cell cycle in the G1/G0 phase. This assumption was confirmed by cell cycle analysis using the fluorescent dye propidium iodide. Thus, the cytotoxic effect of the tested compounds can be characterized by the induction of apoptosis along the internal pathway associated with mitochondrial dysfunction, cell cycle delay in the G1/G0 phase.

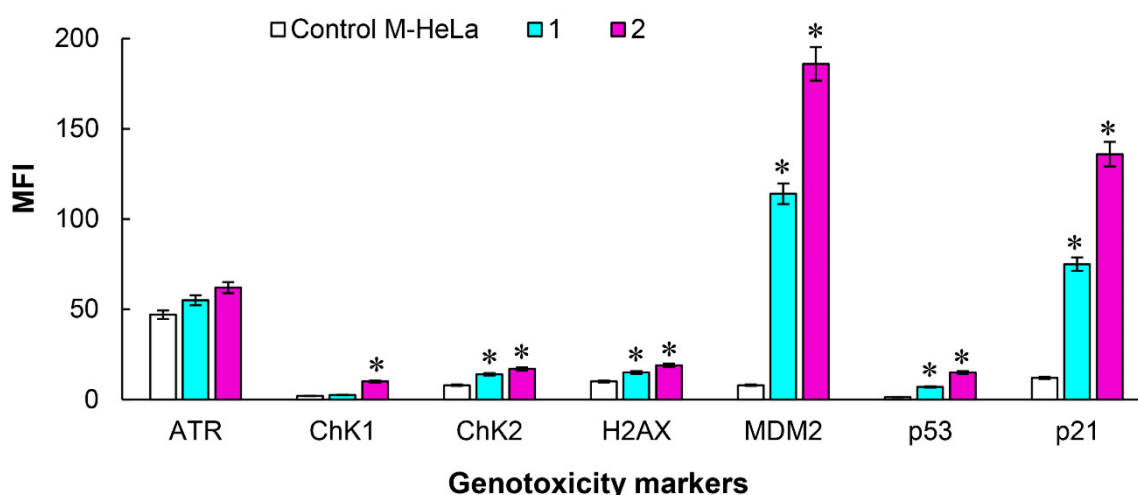


Figure 15. Multiplex analysis of markers DNA damage/genotoxicity in M-HeLa cells treated compound 7. 1—at concentration IC₅₀/2 (6 μM); 2—at concentration IC₅₀ (12 μM). M-HeLa cells untreated with the test substance (control). Data are presented as mean ± SD of three independent experiments * Values indicate $p < 0.05$.

3. Materials and Methods

3.1. Synthesis and Characterisation

All reagents (Acros Organics (Belgium), Alfa Aesar (USA)) were used without further purification. The 1,2,3,4-tetrahydropyrimidine-2-thions [22–26], ethyl (Z)-2-(2-hydroxybenzylidene)-7-methyl-3-oxo-5-phenyl-2,3-dihydro-5H-thiazolo[3,2-*a*]pyrimidine-6-carboxylate 7 [17], ethyl (Z)-2-(4-hydroxybenzylidene)-7-methyl-3-oxo-5-phenyl-2,3-dihydro-5H-thiazolo[3,2-*a*]pyrimidine-6-carboxylate 13 [30], ethyl (Z)-2-(2-hydroxybenzylidene)-5-(4-methoxyphenyl)-7-methyl-3-oxo-2,3-dihydro-5H-thiazolo[3,2-*a*]pyrimidine-6-carboxylate 8 [17] and ethyl (Z)-2-(2-hydroxybenzylidene)-5-(2-methoxyphenyl)-7-methyl-3-oxo-2,3-dihydro-5H-thiazolo[3,2-*a*]pyrimidine-6-carboxylate 9 [17] were synthesized according reported methods.

NMR experiments were performed on Bruker Avance instruments with an operating frequency of 400, 500, and 600 MHz for shooting ^1H and ^{13}C NMR spectra. Chemical shifts were determined relative to the signals of residual protons of the CDCl_3 or $\text{DMSO-}d_6$ solvents.

IR spectra in KBr tablets were recorded on a Bruker Vector-22.

Electrospray ionization (ESI) mass spectra were obtained using a Bruker AmaZon X ion trap mass spectrometer. Melting points were determined on a BOETIUS melting table with an RNMK 05 imaging device.

3.1.1. General Method for Compounds 10–15 Preparation

The hydrochloride of the appropriate thiazolo[3,2-*a*]pyrimidine (1 mol) was mixed with CHCl_3 (50 mL) and water (50 mL) solution containing 1 mol NaOH and stirred for 30 min at room temperature. Then, aromatic aldehyde (2- or 4-hydroxybenzaldehyde) (1 mol) and a catalytic amount (several drops) of pyrrolidine were added. A resulting mixture was stirred for 6 h under refluxing conditions. After cooling, the formed precipitate was filtered off, washed with ethanol, and purified by recrystallization from methanol followed by drying in vacuum for 2 h at 100 °C temperature affording a pure product.

Ethyl (Z)-2-(2-hydroxybenzylidene)-7-methyl-5-(3-nitrophenyl)-3-oxo-2,3-dihydro-5H-thiazolo[3,2-*a*]pyrimidine-6-carboxylate 10. Yield 87%, orange powder, mp 187–189 °C. IR (KBr, cm^{-1}): 3272 (OH); 1704 (C=O); 1595, 1535 (C=N); 1158, 748 (C-S). ^1H NMR (400 MHz, $\text{DMSO-}d_6$, 25 °C) δ_{H} ppm: 1.11 (t, $J = 7.1$ Hz, 3H, OCH_2CH_3), 2.42 (s, 3H, CH_3), 4.00–4.08 (m, 2H, OCH_2CH_3), 6.18 (s, 1H, CH-Ar), 6.94–6.98 (m, 2H, CH (Ar)), 7.30–7.38 (m, 2H, CH (Ar)), 7.66–7.71 (m, 1H, CH (Ar)), 7.78–7.80 (m, 1H, CH (Ar)), 7.97 (s, 1H, C=CH), 8.13 (s, 1H, CH (Ar)), 8.17–8.18 (m, 1H, CH (Ar)), 10.62 (br.s, 1H, OH). ^{13}C NMR (100 MHz, $\text{DMSO-}d_6$, 25 °C) δ_{C} ppm: 14.3, 23.1, 55.0, 60.7, 107.9, 116.7, 118.5, 120.1, 120.3, 120.4, 123.0, 123.9, 129.4, 131.0, 133.3, 134.7, 148.2, 156.8, 157.7, 165.1, 165.7. MS (ESI), m/z : 466 [M + H] $^+$ (see Figures S1–S4).

(Z)-6-benzoyl-2-(2-hydroxybenzylidene)-5-(2-methoxyphenyl)-7-methyl-5H-thiazolo[3,2-*a*]pyrimidin-3(2H)-one 11. Yield 45%, orange powder, mp 167–169 °C. IR (KBr, cm^{-1}): 3448 (OH); 1624 (C=O); 1572 (C=N); 1487; 1272; 751 (C-S). ^1H NMR (400 MHz, $\text{DMSO-}d_6$, 25 °C) δ_{H} ppm: 1.70 (s, 3H, CH_3), 3.62 (s, 3H, OCH_3), 6.27 (s, 1H, CH-Ar), 6.85–6.88 (m, 1H, CH (Ar)), 6.95–7.00 (m, 4H, CH (Ar)), 7.21–7.24 (m, 1H, CH (Ar)), 7.32–7.35 (m, 1H, CH (Ar)), 7.40–7.48 (m, 3H, CH (Ar)), 7.58–7.61 (m, 3H, CH (Ar)), 7.94 (s, 1H, C=CH), 10.53 (s, 1H, OH). ^{13}C NMR (100 MHz, $\text{DMSO-}d_6$, 25 °C) δ_{C} ppm: 22.2, 54.2, 55.8, 112.2, 116.2, 116.6, 118.9, 120.3, 120.5, 121.0, 127.0, 127.6, 128.6, 128.7, 129.0, 129.3, 130.3, 132.9, 133.7, 138.4, 142.9, 154.7, 157.0, 157.6, 165.0, 195.8. MS (ESI), m/z : 483 [M + H] $^+$ (see Figures S5–S8).

Ethyl (Z)-5-(4-bromophenyl)-2-(2-hydroxybenzylidene)-7-methyl-3-oxo-2,3-dihydro-5H-thiazolo[3,2-*a*]pyrimidine-6-carboxylate 12. Yield 88%, orange powder, mp 201–203 °C. IR (KBr, cm^{-1}): 3222 (OH); 1704 (C=O); 1595; 1553 (C=N); 1163. ^1H NMR (500 MHz, $\text{DMSO-}d_6$, 25 °C) δ_{H} ppm: 1.14 (t, $J = 7.1$ Hz, 3H, OCH_2CH_3), 2.39 (s, 3H, CH_3), 4.02–4.09 (m, 2H, OCH_2CH_3), 6.03 (s, 1H, CH-Ar), 6.95–6.98 (m, 2H, CH (Ar)), 7.27 (d, $J = 8.5$ Hz, 2H, CH (Ar)), 7.31–7.38 (m, 2H, CH (Ar)), 7.56 (d, $J = 8.5$ Hz, 2H, CH (Ar)), 7.97 (s, 1H, C=CH). ^{13}C NMR (100 MHz, $\text{DMSO-}d_6$, 25 °C) δ_{C} ppm: 14.9, 23.5, 55.4, 61.2, 109.0, 117.2, 119.1,

120.7, 120.7, 120.8, 122.8, 129.7, 130.8, 132.6, 133.7, 140.7, 152.7, 157.0, 158.3, 165.5, 165.7. MS (ESI), m/z : 499, 501 $[M + H]^+$ (see Figures S9–S12).

Ethyl (Z)-5-(4-bromophenyl)-2-(4-hydroxybenzylidene)-7-methyl-3-oxo-2,3-dihydro-5H-thiazolo[3,2-*a*]pyrimidine-6-carboxylate 14. Yield 88%, orange powder, mp 207–209 °C. IR (KBr, cm^{-1}): 3413 (OH); 1717 (C=O); 1585 (C=N); 1515; 1160. ^1H NMR (600 MHz, DMSO-d_6 , 25 °C) δ_{H} ppm: 1.13 (t, $J = 7$ Hz, 3H, OCH_2CH_3), 2.38 (s, 3H, CH_3), 4.03–4.08 (m, 2H, OCH_2CH_3), 6.01 (s, 1H, CH-Ar), 6.92 (d, $J = 8.4$ Hz, 2H, CH (Ar)), 7.25 (d, $J = 8$ Hz, 2H, CH (Ar)), 7.46 (d, $J = 8.4$ Hz, 2H, CH (Ar)), 7.54 (d, $J = 8$ Hz, 2H, CH (Ar)), 7.69 (s, 1H, C=CH). ^{13}C NMR (100 MHz, DMSO-d_6 , 25 °C) δ_{C} ppm: 14.4, 22.8, 54.8, 60.7, 108.3, 115.4, 116.9, 122.2, 124.1, 130.2, 132.1, 133.1, 134.3, 140.3, 152.3, 156.6, 160.8, 165.0, 165.3. MS (ESI), m/z : 499, 501 $[M + H]^+$ (see Figures S13–S15).

Ethyl (Z)-2-(4-hydroxybenzylidene)-7-methyl-5-(3-nitrophenyl)-3-oxo-2,3-dihydro-5H-thiazolo[3,2-*a*]pyrimidine-6-carboxylate 15. Yield 84%, orange powder, mp 190–192 °C. IR (KBr, cm^{-1}): 3048 (OH); 1717 (C=O); 1585; 1515; 1160. ^1H NMR (500 MHz, DMSO-d_6 , 25 °C) δ_{H} ppm: 1.11 (t, $J = 7.1$ Hz, 3H, OCH_2CH_3), 2.42 (s, 3H, CH_3), 3.99–4.08 (m, 2H, OCH_2CH_3), 6.17 (s, 1H, CH-Ar), 6.92 (d, $J = 8.7$ Hz, 2H, CH (Ar)), 7.47 (d, $J = 8.7$ Hz, 2H, CH (Ar)), 7.66–7.69 (m, 1H, CH (Ar)), 7.70 (s, 1H, C=CH), 7.77–7.79 (m, 1H, CH (Ar)), 8.12–8.13 (m, 1H, CH (Ar)), 8.16–8.18 (m, 1H, CH (Ar)), 10.39 (br.s, 1H, OH). ^{13}C NMR (100 MHz, DMSO-d_6 , 25 °C) δ_{C} ppm: 14.3, 23.1, 55.0, 60.7, 107.7, 115.3, 116.9, 122.9, 123.9, 124.1, 131.0, 133.1, 134.5, 134.6, 142.8, 148.1, 153.1, 156.9, 160.9, 165.1. MS (ESI), m/z : 466 $[M + H]^+$ (see Figures S16–S18).

3.1.2. Crystallization Conditions

Crystals of **11**, **12**, **13**, and **14** suitable for X-ray diffraction study were obtained by slow evaporation of ethanol solution (25 mL) containing 0.02 mol of dissolved compound after 5 days.

Crystals of solvates **12-DMSO** and **14-DMSO** suitable for X-ray diffraction study were obtained by slow evaporation of DMSO solution (10 mL) containing 0.02 mol of dissolved compound after 7 days.

Crystals of solvate **10-MeOH** suitable for X-ray diffraction study were obtained by slow evaporation of MeOH solution (15 mL) containing 0.02 mol of the dissolved compound after 3 days.

3.1.3. Single Crystal X-ray Diffraction

The X-ray diffraction study of **12** was carried out at the “Belok/XSA” beamline of the Kurchatov Synchrotron Radiation Source [31,32]. Diffraction patterns were collected using Mardtb goniometer (marXperts GmbH, Werkstraße 3, 22844 Norderstedt, Germany) equipped with Rayonix SX165 CCD (Rayonix LLC., 1880 Oak Ave UNIT 120, Evanston, IL 60201, USA) 2D positional sensitive CCD detector ($\lambda = 0.7450$ Å, φ -scanning in 1.0° steps). All data were collected at 100(2) K.

X-ray diffraction analysis of **10-MeOH**, **11**, **12-DMSO**, **13**, **14**, and **14-DMSO** was performed on a Bruker D8 QUEST automatic three-circle diffractometer with a PHOTON III two-dimensional detector and an I μ S DIAMOND microfocus X-ray tube ($\lambda[\text{Mo K}\alpha] = 0.71073$ Å) at cooling conditions. Data collection and processing of diffraction data were performed using APEX3 software package.

All structures were solved by the direct method using the SHELXT program [33] and refined by the full-matrix least squares method over F^2 using the SHELXL program [34]. All calculations were performed in the WinGX software package [35], the calculation of the geometry of molecules and intermolecular interactions in crystals was carried out using the PLATON program [36], the drawings of molecules were performed using the ORTEP-3 [35] and MERCURY [37] programs.

Non-hydrogen atoms were refined in the anisotropic approximation. The positions of the hydrogen atoms H(O) were determined using difference Fourier maps, and these atoms were refined isotropically. The remaining hydrogen atoms are placed in geometrically

calculated positions and included in the refinement in the “riding” model. The crystal of compound **9**, **12**, and **14** is a solvate with DMSO (1:1); crystal of compound **9**—solvate with methanol (1:1). Crystallographic data of structures **9–14** were deposited at the Cambridge Crystallographic Data Center, registration numbers and the most important characteristics are given in Table 3.

Table 3. Crystallographic data for studied compounds.

Compound	10-MeOH	11	12	12-DMSO
Molecular formula	C ₂₃ H ₁₉ N ₂ O ₅ S, CH ₄ O	C ₂₈ H ₂₂ N ₂ O ₄ S	C ₂₃ H ₁₉ BrN ₂ O ₄ S	C ₂₃ H ₁₉ BrN ₂ O ₄ S, C ₂ H ₆ OS
Sum Formula	C ₂₄ H ₂₃ N ₂ O ₅ S	C ₂₈ H ₂₂ N ₂ O ₄ S	C ₂₃ H ₁₉ BrN ₂ O ₄ S	C ₂₆ H ₂₈ N ₂ O ₆ S ₂
Formula Weight	497.51	482.54	499.36	577.49
Crystal System	triclinic	triclinic	triclinic	triclinic
Space group	<i>P</i> -1 (<i>P1bar</i>)	<i>P</i> -1 (<i>P1bar</i>)	<i>P</i> -1 (<i>P1bar</i>)	<i>P</i> -1 (<i>P1bar</i>)
Temp. of measurement, K	100(2)	105(2)	100(2)	105(2)
Cell parameters	<i>a</i> = 9.4229(5) Å, <i>b</i> = 9.4636(5) Å, <i>c</i> = 12.8810(7) Å; α = 82.651(2)° β = 89.551(2)° γ = 77.443(2)°	<i>a</i> = 9.7165(8) Å, <i>b</i> = 10.1644(9) Å, <i>c</i> = 13.4602(12) Å; α = 101.395(3)° β = 99.097(3)° γ = 113.423(3)°	<i>a</i> = 7.7700(16) Å, <i>b</i> = 11.950(2) Å, <i>c</i> = 12.540(3) Å; α = 64.59(3)° β = 82.44(3)° γ = 86.70(3)°	<i>a</i> = 8.5364(2) Å, <i>b</i> = 11.8152(3) Å, <i>c</i> = 13.4137(4) Å; α = 103.604(1)° β = 106.947(1)° γ = 92.508(1)°
V [Å ³]	1111.74(10)	1153.65(18)	1042.6(5)	1248.63(6)
Z and Z'	2 and 1	2 and 1	2 and 1	2 and 1
D(calc) [g/cm ³]	1.486	1.389	1.591	1.536
λ (Å)	(MoK α) 0.71073	(MoK α) 0.71073	0.7450 (synchrotron)	(MoK α) 0.71073
μ [/mm]	0.199	0.180	2.355	1.853
<i>F</i> (000)	520	504	508	592
Theta Min-Max [Deg]	2.2–28.0°	2.3–30.0°	1.9–31.0°	1.8–32.0°
Reflections measured	41,825	89,193	20,991	44,055
Independent reflections	5357	6713	5717	8644
Observed reflections [<i>I</i> > 2 σ (<i>I</i>)]	4506	5883	5297	7568
Goodness of fit	1.138	1.030	1.076	1.048
<i>R</i> [<i>I</i> > 2 σ (<i>I</i>)]	<i>R</i> 1 = 0.0391, <i>wR</i> 2 = 0.1137	<i>R</i> 1 = 0.0340, <i>wR</i> 2 = 0.0956	<i>R</i> 1 = 0.0326, <i>wR</i> 2 = 0.0867	<i>R</i> 1 = 0.0356, <i>wR</i> 2 = 0.1004
<i>R</i> (all reflections)	<i>R</i> 1 = 0.0491, <i>wR</i> 2 = 0.1189	<i>R</i> 1 = 0.0397, <i>wR</i> 2 = 0.0985	<i>R</i> 1 = 0.0361, <i>wR</i> 2 = 0.0901	<i>R</i> 1 = 0.0418, <i>wR</i> 2 = 0.1036
Max. and Min. Resd. Dens. [e/Å ⁻³]	0.52 and −0.23	0.46 and −0.27	0.44 and −0.86	1.19 and −0.51
Depositor numbers in CCDC	2,213,096	2,213,093	2,213,097	2,213,094
Compound	13	14	14-DMSO	
Molecular formula	C ₂₃ H ₂₀ N ₂ O ₄ S	C ₂₃ H ₁₉ BrN ₂ O ₄ S	C ₂₃ H ₁₉ BrN ₂ O ₄ S, C ₂ H ₆ OS	
Sum Formula	C ₂₃ H ₂₀ N ₂ O ₄ S	C ₂₃ H ₁₉ BrN ₂ O ₄ S	C ₂₆ H ₂₈ N ₂ O ₆ S ₂	
Formula Weight	420.47	499.36	577.49	
Crystal System	monoclinic	monoclinic	triclinic	
Space group	<i>Pc</i>	<i>P</i> 2 ₁ / <i>n</i>	<i>P</i> -1 (<i>P1bar</i>)	

Table 3. Cont.

Compound	10-MeOH	11	12	12-DMSO
Temp. of measurement, K	110(2)	110(2)		105(2)
Cell parameters	$a = 11.0059(15) \text{ \AA}$, $b = 13.6530(15) \text{ \AA}$, $c = 14.8440(18) \text{ \AA}$; $\beta = 109.743(3)^\circ$	$a = 11.3394(5) \text{ \AA}$, $b = 14.2710(7) \text{ \AA}$, $c = 13.6906(6) \text{ \AA}$; $\beta = 104.046(2)^\circ$		$a = 8.8459(4) \text{ \AA}$, $b = 11.2404(4) \text{ \AA}$, $c = 12.8542(5) \text{ \AA}$; $\alpha = 89.785(2)^\circ$; $\beta = 88.746(2)^\circ$; $\gamma = 83.140(2)^\circ$
V [\AA^3]	2099.4(4)	2149.24(17)		1268.66(9)
Z and Z'	4 and 2	4 and 1		2 and 1
D(calc) [g/cm^3]	1.330	1.543		1.512
λ (\AA)	(MoK α) 0.71073	(MoK α) 0.71073		(MoK α) 0.71073
μ [$/\text{mm}$]	0.186	2.043		1.824
F(000)	880	1016		592
Theta Min-Max [Deg]	1.5–26.6°	2.1–30.0°		1.8–30.0°
Reflections measured	69,218	104,197		89,171
Independent reflections	8626	6257		7381
Observed reflections [$I > 2\sigma(I)$]	6008	4741		6684
Goodness of fit	1.062	1.009		1.027
R [$I > 2\sigma(I)$]	R1 0.0576, wR2 = 0.1249	R1 = 0.0347, wR2 = 0.0713		R1 = 0.0304, wR2 = 0.0761
R (all reflections)	R1 = 0.1017, wR2 = 0.1417	R1 = 0.0578, wR2 = 0.0783		R1 = 0.0355, wR2 = 0.0786
Max. and Min. Resd. Dens. [$\text{e}/\text{\AA}^{-3}$]	0.35 and −0.55	0.55 and −0.41		0.68 and −0.61
Flack parameter	−0.35(8) (twin, BASF 0.52081)	-		-
Depositor numbers in CCDC	2,213,099	2,213,095		2,213,098

3.2. Biological Study

3.2.1. Cells and Materials

For the experiments, tumor cell cultures of M-HeLa clone 11 (epithelioid carcinoma of the cervix, subline HeLa., clone M-HeLa), HuTu 80, human duodenal adenocarcinoma, MCF7—human breast adenocarcinoma (pleural fluid) collected from Institute of Cytology, Russian Academy of Sciences (St. Petersburg, Russia); PC3—prostate adenocarcinoma cell line collected from ATCC (American Type Cell Collection, Manassas, VA, USA; CRL 1435; human liver cells (Chang liver) and the Research Institute of Virology of the Russian Academy of Medical Sciences (Moscow, Russia) were used for cytotoxicity analysis.

3.2.2. MTT Assay

The cytotoxic effect on cells was determined using the colorimetric method of cell proliferation—the MTT test. NADP-H-dependent cellular oxidoreductase enzymes can, under certain conditions, reflect the number of viable cells. These enzymes are able to reduce the tetrazolium dye (MTT)—3-(4,5-dimethylthiazol-2-yl)-2,5-diphenyl-tetrazolium bromide to insoluble blue-violet formazan, which crystallizes inside the cell. The amount of formazan formed is proportional to the number of cells with active metabolism. Cells were seeded on a 96-well Nunc plate at a concentration of 5×10^3 cells per well in a volume of

100 μL of medium and cultured in a CO_2 incubator at 37°C until a monolayer was formed. Then the nutrient medium was removed and 100 μL of solution of the test drug in the given dilutions was added to the wells, which were prepared directly in the nutrient medium with the addition of 5% DMSO to improve solubility. After 48 h of incubation of the cells with the tested compounds, the nutrient medium was removed from the plates and 100 μL of the nutrient medium without serum with MTT at a concentration of 0.5 mg/mL was added and incubated for 4 h at 37°C . Formazan crystals were added to 100 μL of DMSO. Optical density was recorded at 540 nm on an Invitrologic microplate reader (Novosibirsk, Russia). The experiments for all compounds were repeated three times.

3.2.3. Induction of Apoptotic Effects by Test Compounds

Flow Cytometry Assay

Cell Culture. M-HeLa cells at 1×10^6 cells/well in a final volume of 2 mL were seeded into six-well plates. After 48 h of incubation, various concentrations of compound 7 were added to the wells.

Cell Apoptosis Analysis. The cells were harvested at 2000 rpm for 5 min and then washed twice with ice-cold PBS, followed by resuspension in binding buffer. Next, the samples were incubated with 5 μL of annexin V-Alexa Fluor 647 (Sigma-Aldrich, St. Louis, MO, USA) and 5 μL of propidium iodide for 15 min at room temperature in the dark. Finally, the cells were analyzed by flow cytometry (Guava easy Cyte, MERCK, Kenilworth, NJ, USA) within 1 h. The experiments were repeated three times.

Mitochondrial Membrane Potential. Cells were harvested at 2000 rpm for 5 min and then washed twice with ice-cold PBS, followed by resuspension in JC-10 (10 $\mu\text{g}/\text{mL}$) and incubation at 37°C for 10 min. After the cells were rinsed three times and suspended in PBS, the JC-10 fluorescence was observed by flow cytometry (Guava easy Cyte, MERCK, Kenilworth, NJ, USA).

3.2.4. Detection of Intracellular ROS

M-HeLa cells were incubated with compound 7 at concentrations of $\text{IC}_{50}/2$ and IC_{50} for 48 h. ROS generation was investigated using flow cytometry assay and CellROX[®] Deep Red flow cytometry kit. For this, M-HeLa cells were harvested at 2000 rpm for 5 min and then washed twice with ice-cold PBS, followed by resuspension in 0.1 mL of medium without FBS, to which 0.2 μL of CellROX[®] Deep Red was added and incubated at 37°C for 30 min. After three times washing the cells and suspending them in PBS, the production of ROS in the cells was immediately monitored using flow cytometer (Guava easy Cyte, MERCK, Kenilworth, NJ, USA).

3.2.5. Multiplex Analysis of Markers DNA Damage/Genotoxicity

The studies were carried out according to the standard protocol. M-HeLa cells were incubated for 24 h with the test substance. Cells were lysed in MILLIPLEX[®] MAP Lysis buffer containing protease inhibitors. A total of 20 μg of total protein of each lysate diluted in MILLIPLEX[®] MAP Assay Buffer 2 was analyzed according to the analysis protocol (the lysate was incubated at 4°C overnight). The mean fluorescence intensity (MFI) was detected using Luminex[®] system, MERCK, Kenilworth, NJ, USA.

Statistical Analysis

The IC_{50} values were calculated using the online calculator MLA-Quest Graph[™] IC_{50} Calculator AAT Bioquest, Inc., 14 February 2021. Statistical analysis was performed using the Mann–Whitney test ($p < 0.05$). Tabular and graphical data contain the averages and standard error.

4. Conclusions

Synthesis of new 2-(2- and 4-hydroxybenzylidene)thiazolo[3,2-*a*]pyrimidine derivatives 10–15 containing phenyl, *m*-nitrophenyl, *p*-bromophenyl, and *o*-anisyl substituents

at the C5 atom was successfully achieved in high yields. The single crystal X-ray diffraction study revealed that the supramolecular motif in the crystalline phase of the obtained compounds can be controlled by adjusting the interplay between various types of non-covalent interactions such as H-, Br- π , O- π , π - π bonding through the rational choice of the substituents at C2, C5, and C6 atoms. Depending on the used 2- or 4-hydroxybenzylidene derivatives, the self-assembly pathway leads to the formation of racemic H-bonded dimers (**11**, **12**) or infinite 1D homochiral chains (**13**, **14**), respectively, which can be explained by the close disposition of H-bond donor and H-bond acceptor observed for **11** and **12**, and relatively high H-accepting ability of N8 pyrimidine atom in the case of **13** and **14**. Moreover, the 1D chains can be generated for 2-hydroxybenzylidene by involving protic EtOH or MeOH acting as bridges in intermolecular H-bonding between the obtained heterocycles (**10-MeOH**). It was demonstrated that upon crystal packing, the relatively weak Br- π , O- π , and π - π interactions also play a significant role which can be enhanced by switching off the intermolecular H-bonding when DMSO molecules are involved in coordination with OH-donor group.

A series composed of new compounds 2-(2- and 4-hydroxybenzylidene)thiazolo[3,2-*a*]pyrimidine derivatives **10–15** and their earlier reported analogues **7–9** were tested *in vitro* as antitumor agents. The studied compounds showed high or moderate activity against a number of cancer lines of various genesis and demonstrated moderate cytotoxicity against normal liver cells. The most significant results of the studied compounds were shown in relation to the cell lines of cervical carcinoma (M-HeLa) and human duodenal adenocarcinoma (HuTu 80). Their cytotoxic effect was confirmed by comparing with drug sorafenib, and compound **7** has demonstrated two times higher efficiency. According to the calculated indices of selectivity of cytotoxic action, compound **7** also demonstrates better selectivity with respect to the M-HeLa and HuTu 80 cell lines. Using the flow cytometry method and multiplex analysis of DNA damage/genotoxicity markers, it was shown that the cytotoxic effect of the tested compound **7** can be characterized by the induction of apoptosis along the internal pathway associated with mitochondrial dysfunction, cell cycle delay in the G1/G0 phase. The design of new thiazolo[3,2-*a*]pyrimidines exhibiting higher anti-tumor activity with simultaneously low normal cells toxicity is in progress.

Supplementary Materials: The following supporting information can be downloaded at: <https://www.mdpi.com/article/10.3390/molecules27227747/s1>. Figure S1: ^1H NMR spectrum of compound **10** (DMSO- d_6 , 400 MHz, 25 °C). Figure S2: ^{13}C NMR spectrum of compound **10** (DMSO- d_6 , 100 MHz, 25 °C). Figure S3: ESI MS spectrum of compound **10** (ion polarity: positive). Figure S4: IR spectrum of compound **10** (KBr tablet). Figure S5: ^1H NMR spectrum of compound **11** (DMSO- d_6 , 400 MHz, 25 °C). Figure S6: ^{13}C NMR spectrum of compound **11** (DMSO- d_6 , 100 MHz, 25 °C). Figure S7: ESI MS spectrum of compound **11** (ion polarity: positive). Figure S8: IR spectrum of compound **11** (KBr tablet). Figure S9: ^1H NMR spectrum of compound **12** (DMSO- d_6 , 400 MHz, 25 °C). Figure S10: ^{13}C NMR spectrum of compound **12** (DMSO- d_6 , 100 MHz, 25 °C). Figure S11: ESI MS spectrum of compound **12** (ion polarity: positive). Figure S12: IR spectrum of compound **12** (KBr tablet). Figure S13: ^1H NMR spectrum of compound **14** (DMSO- d_6 , 600 MHz, 25 °C). Figure S14: ^{13}C NMR spectrum of compound **14** (DMSO- d_6 , 100 MHz, 25 °C). Figure S15: IR spectrum (KBr tablet) and ESI MS spectrum (ion polarity: positive) of compound **14**. Figure S16: ^1H NMR spectrum of compound **15** (DMSO- d_6 , 500 MHz, 25 °C). Figure S17: ^{13}C NMR spectrum of compound **15** (DMSO- d_6 , 100 MHz, 25 °C). Figure S18: ESI MS spectrum of compound **15** (ion polarity: positive). Figure S19: Fragment of crystal packing of **11-DMSO** showing the intermolecular H-, Br/ π -, and π - π bonding (red, brown, and blue dotted lines, respectively). Figure S20: Fragment of crystal packing of **14** showing the intermolecular H-, Br/ π -, and π - π bonding (red, brown, and blue dotted lines, respectively). Figure S21: Fragment of crystal packing of **14-DMSO** showing the intermolecular H-, Br/ π -, and π - π bonding (red, brown, and blue dotted lines, respectively). Table S1: Bond distances and angles of asymmetric C5 atom in studied compounds established by SCXRD. Table S2: Selected bond distances and dihedral angles for studied compounds established by SCXRD. Table S3: H-bond distances presenting in crystals of studied compounds.

Author Contributions: Conceptualization, I.S.A., A.S.A. and S.E.S.; methodology, A.S.O. and I.A.L.; validation, A.S.A., I.A.L. and A.S.O.; formal analysis, I.A.L., A.S.O. and P.V.D.; investigation, E.R.G., A.A.N., A.S.A., I.A.L., S.K.A. and A.P.L.; resources, P.V.D., A.D.V. and I.A.L.; data curation, A.S.A., I.S.A., S.E.S. and A.D.V.; writing—original draft preparation, A.S.A., I.A.L., A.S.O., I.S.A., S.E.S. and A.D.V.; writing—review and editing, A.S.A., I.A.L., A.S.O., I.S.A., S.E.S. and A.D.V.; visualization, A.S.O. and A.S.A.; supervision, I.S.A. and S.E.S.; project administration, A.S.A., I.S.A. and S.E.S.; funding acquisition, I.S.A. All authors have read and agreed to the published version of the manuscript.

Funding: This work was funded by financial support from government assignment for the Arbuzov Institute of Organic and Physical Chemistry, FRC Kazan Scientific Center, Russian Academy of Sciences (122011800132-5).

Institutional Review Board Statement: Not applicable.

Informed Consent Statement: Not applicable.

Data Availability Statement: The data presented in this study are contained within the article or in Supplementary Materials, or are available on request from the corresponding author Igor Antipin.

Acknowledgments: The authors are grateful to the Assigned Spectral-Analytical Center of Shared Facilities for Study of Structure, Composition and Properties of Substances and Materials of the Federal Research Center of Kazan Scientific Center of Russian Academy of Sciences (CSF-SAC FRC KSC RAS) for technical support.

Conflicts of Interest: The authors declare no conflict of interest.

Sample Availability: Samples of the compounds 7–15 are available from the authors.

References

1. Venkatesh, T.; Upendranath, K.; Nayaka, Y.A. Development of electrochemical and optoelectronic performance of new 7-[[1H-indol-3-ylmethylidene]amino]-4-methyl-2H-chromen-2-one dye. *J. Solid State Electrochem.* **2021**, *25*, 1237–1244. [[CrossRef](#)]
2. Sukanya, S.H.; Venkatesh, T.; Rao, S.A.; Joy, M.N. Efficient L-Proline catalyzed synthesis of some new (4-substituted-phenyl)-1,5-dihydro-2H-pyrimido[4,5-d][1,3]thiazolo[3,2-a]pyrimidine-2,4(3H)-diones bearing thiazolopyrimidine derivatives and evaluation of their pharmacological activities. *J. Mol. Struct.* **2022**, *1247*, 131324. [[CrossRef](#)]
3. Nagaraju, P.; Reddy, P.N.; Padmaja, P.; Ugale, V.G. Microwave-Assisted Synthesis of Thiazole/Benzothiazole Fused Pyranopyrimidine Derivatives and Evaluation of their Biological Activity. *Lett. Org. Chem.* **2021**, *18*, 49–57. [[CrossRef](#)]
4. El-Shahat, M.; Salama, M.; El-Faragy, A.F.; Ali, M.M.; Ahmed, D.M. Effective pharmacophore for CDC25 phosphatases enzyme inhibitors: Newly synthesized bromothiazolopyrimidine derivatives. *Mini Rev. Med. Chem.* **2021**, *21*, 118–131. [[CrossRef](#)] [[PubMed](#)]
5. Nagaraju, P.; Reddy, P.N.; Padmaja, P.; Ugale, V.G. Synthesis, Antiproliferative Activity and Molecular Docking of New Thiazole/Benzothiazole Fused Pyranopyrimidine Derivatives. *Lett. Org. Chem.* **2020**, *17*, 951–958. [[CrossRef](#)]
6. Mohamed, S.F.; Abbas, E.M.; Khalaf, H.S.; Farghaly, T.A.; Abd El-Shafy, D.N. Triazolopyrimidines and thiazolopyrimidines: Synthesis, anti-HSV-1, cytotoxicity and mechanism of action. *Mini Rev. Med. Chem.* **2018**, *18*, 794–802. [[CrossRef](#)]
7. Abdel-Hafez, N.A.; Mohamed, S.F.; El-Hag, F.A.; Hawas, U.W.; Awad, H.M. Synthesis and cytotoxicity evaluation of some new pyrimidinethione and thiazolopyrimidine derivatives linked to N-propylpiperidone. *Der Pharma Chem.* **2016**, *8*, 1–10.
8. Keshari, K.A.; Singh, K.A.; Saha, S. Bridgehead nitrogen thiazolo [3, 2-a] pyrimidine: A privileged structural framework in drug discovery. *Mini Rev. Med. Chem.* **2017**, *17*, 1488–1499. [[CrossRef](#)]
9. Sung, H.; Ferlay, J.; Siegel, R.L.; Laversanne, M.; Soerjomataram, I.; Jemal, A.; Bray, F. Global cancer statistics 2020: GLOBOCAN estimates of incidence and mortality worldwide for 36 cancers in 185 countries. *CA Cancer J. Clin.* **2021**, *71*, 209–249. [[CrossRef](#)]
10. Gali, R.; Banothu, J.; Porika, M.; Velpula, R.; Hnamte, S.; Bavantula, R.; Abbagani, S.; Busi, S. Indolylmethylene benzo[h]thiazolo[2, 3-b]quinazolinones: Synthesis, characterization and evaluation of anticancer and antimicrobial activities. *Bioorg. Med. Chem. Lett.* **2014**, *24*, 4239–4242. [[CrossRef](#)]
11. Studzińska, R.; Kołodziejka, R.; Redka, M.; Modzelewska-Banachiewicz, B.; Augustyńska, B. Lipophilicity study of thiazolo[3, 2-a]pyrimidine derivatives as potential bioactive agents. *J. Braz. Chem. Soc.* **2016**, *27*, 1587–1593. [[CrossRef](#)]
12. Zhou, B.; Li, X.; Li, Y.; Xu, Y.; Zhang, Z.; Zhou, M.; Zhang, X.; Liu, Z.; Zhou, J.; Cao, C.; et al. Discovery and Development of Thiazolo[3, 2-a]pyrimidinone Derivatives as General Inhibitors of Bcl-2 Family Proteins. *ChemMedChem* **2011**, *6*, 904–921. [[CrossRef](#)] [[PubMed](#)]
13. Feng, Y.; Ding, X.; Chen, T.; Chen, L.; Liu, F.; Jia, X.; Luo, X.; Shen, X.; Chen, K.; Jiang, H.; et al. Design, synthesis, and interaction study of quinazoline-2(1H)-thione derivatives as novel potential Bcl-xL inhibitors. *J. Med. Chem.* **2010**, *53*, 3465–3479. [[CrossRef](#)] [[PubMed](#)]

14. Kolb, S.; Mondésert, O.; Goddard, M.L.; Jullien, D.; Villoutreix, B.O.; Ducommun, B.; Garbay, C.; Braud, E. Development of novel thiazolopyrimidines as CDC25B phosphatase inhibitors. *ChemMedChem Chem. Enabling Drug Discov.* **2009**, *4*, 633–648. [[CrossRef](#)]
15. Jin, C.H.; Jun, K.Y.; Lee, E.; Kim, S.; Kwon, Y.; Kim, K.; Na, Y. Ethyl 2-(benzylidene)-7-methyl-3-oxo-2,3-dihydro-5H-thiazolo[3,2-*a*]pyrimidine-6-carboxylate analogues as a new scaffold for protein kinase casein kinase 2 inhibitor. *Bioorg. Med. Chem.* **2014**, *22*, 4553–4565. [[CrossRef](#)]
16. Agarkov, A.S.; Gabitova, E.R.; Galieva, F.B.; Ovsyannikov, A.S.; Voloshina, A.D.; Shiryayev, A.K.; Litvinov, I.A.; Solovieva, S.E.; Antipin, I.S. Structure and Biological Properties of 2-Phenylhydrazone Derivatives of Thiazolopyrimidines. In *Doklady Chemistry*; Pleiades Publishing: New York, NY, USA, 2022; Volume 503, pp. 45–50.
17. Agarkov, A.S.; Litvinov, I.A.; Gabitova, E.R.; Ovsyannikov, A.S.; Dorovatovskii, P.V.; Shiryayev, A.K.; Solovieva, S.E.; Antipin, I.S. Crystalline State Hydrogen Bonding of 2-(2-Hydroxybenzylidene)Thiazolo[3,2-*a*]Pyrimidines: A Way to Non-Centrosymmetric Crystals. *Crystals* **2022**, *12*, 494. [[CrossRef](#)]
18. Lashmanova, E.A.; Rybakov, V.B.; Shiryayev, A.K. Synthesis of adamantylated pyrimidines using the Biginelli reaction. *Synthesis* **2016**, *48*, 3965–3970.
19. Shiryayev, A.K.; Baranovskaya, N.S.; Eremin, M.S. Synthesis of 5H-thiazolo[3,2-*a*]pyrimidines. *Chem. Heterocycl. Compd.* **2012**, *48*, 1662–1667. [[CrossRef](#)]
20. Shiryayev, A.K.; Kolesnikova, N.G.; Kuznetsova, N.M.; Lashmanova, E.A. Alkylation of tetrahydropyrimidine-2-thions with ethyl chloroacetate. *Chem. Heterocycl. Compd.* **2013**, *49*, 1812–1817.
21. Lashmanova, E.A.; Kiryashkina, A.I.; Slepukhin, P.A.; Shiryayev, A.K. Oxidation of thiazolo[3,2-*a*]pyrimidin-3(2H)-ones with DMSO and Lawesson's reagent. *Tetrahedron Lett.* **2018**, *59*, 1099–1103. [[CrossRef](#)]
22. Lashmanova, E.A.; Agarkov, A.S.; Rybakov, V.B.; Shiryayev, A.K. Rearrangement of thiazolo[3,2-*a*]pyrimidines into triazolo[4,3-*a*]pyrimidines induced by C=N bond reduction. *Chem. Heterocycl. Compd.* **2019**, *55*, 1217–1221. [[CrossRef](#)]
23. Hwang, J.; Li, P.; Smith, M.D.; Warden, C.E.; Sirianni, D.A.; Vik, E.C.; Maier, J.M.; Yehl, C.J.; Sherrill, C.D.; Shimizu, K.D. Tipping the Balance between S- π and O- π Interactions. *J. Am. Chem. Soc.* **2018**, *140*, 13301–13307. [[CrossRef](#)] [[PubMed](#)]
24. Caron, G.; Kihlberg, J.; Ermondi, G. Intramolecular hydrogen bonding: An opportunity for improved design in medicinal chemistry. *Med. Res. Rev.* **2019**, *39*, 1707–1729. [[CrossRef](#)] [[PubMed](#)]
25. Kuhn, B.; Mohr, P.; Stahl, M. Intramolecular hydrogen bonding in medicinal chemistry. *J. Med. Chem.* **2010**, *53*, 2601–2611. [[CrossRef](#)] [[PubMed](#)]
26. Ayoub, M.S.; Wahby, Y.; Abdel-Hamid, H.; Ramadan, E.S.; Teleb, M.; Abu-Serie, M.M.; Noby, A. Design, synthesis and biological evaluation of novel α -acyloxy carboxamides via Passerini reaction as caspase 3/7 activators. *Eur. J. Med. Chem.* **2019**, *168*, 340–356. [[CrossRef](#)]
27. Abdelwahid, E.; Rolland, S.; Teng, X.; Conradt, B.; Hardwick, J.M.; White, K. Mitochondrial involvement in cell death of non-mammalian eukaryotes. *Biochim. Biophys. Acta (BBA)-Mol. Cell Res.* **2011**, *1813*, 597–607. [[CrossRef](#)]
28. Orrenius, S.; Gogvadze, V.; Zhivotovsky, B. Mitochondrial oxidative stress: Implications for cell death. *Annu. Rev. Pharmacol. Toxicol.* **2007**, *47*, 143–183. [[CrossRef](#)]
29. Carbone, R.; Pearson, M.; Minucci, S.; Pelicci, P.G. PML NBs associate with the hMre11 complex and p53 at sites of irradiation induced DNA damage. *Oncogene* **2002**, *21*, 1633–1640. [[CrossRef](#)]
30. Lebedyeva, I.O.; Povstyanoy, M.V.; Ryabitskii, A.B.; Povstyanoy, V.M. Ternary condensation of Biginelli thiones, chloroacetic acid, and aldehydes as an effective approach towards thiazolo[3,2-*a*]pyrimidines and 5-arylidene-thiazolidine-2,4-diones. *J. Heterocycl. Chem.* **2010**, *47*, 368–372. [[CrossRef](#)]
31. Lazarenko, V.A.; Dorovatovskii, P.V.; Zubavichus, Y.V.; Burlov, A.S.; Koshchienko, Y.V.; Vlasenko, V.G.; Khrustalev, V.N. High-throughput small-molecule crystallography at the 'Belok' beamline of the Kurchatov synchrotron radiation source: Transition metal complexes with azomethine ligands as a case study. *Crystals* **2017**, *7*, 325. [[CrossRef](#)]
32. Svetogorov, R.D.; Dorovatovskii, P.V.; Lazarenko, V.A. Belok/XSA diffraction beamline for studying crystalline samples at Kurchatov Synchrotron Radiation Source. *Cryst. Res. Technol.* **2020**, *55*, 1900184. [[CrossRef](#)]
33. Sheldrick, G.M. SHELXT—Integrated space-group and crystal-structure determination. *Acta Crystallogr. Sect. A Found. Adv.* **2015**, *71*, 3–8. [[CrossRef](#)] [[PubMed](#)]
34. Sheldrick, G.M. Crystal structure refinement with SHELXL. *Acta Crystallogr. Sect. C* **2015**, *71*, 3–8. [[CrossRef](#)] [[PubMed](#)]
35. Farrugia, L.J. WinGX and ORTEP for Windows: An update. *J. Appl. Crystallogr.* **2012**, *45*, 849–854. [[CrossRef](#)]
36. Spek, A.L. Structure validation in chemical crystallography. *Acta Crystallogr. Sect. D Biol. Crystallogr.* **2009**, *65*, 148–155. [[CrossRef](#)] [[PubMed](#)]
37. Macrae, C.F.; Edgington, P.R.; McCabe, P.; Pidcock, E.; Shields, G.P.; Taylor, R.; Towler, M.; Streek, J.V.D. Mercury: Visualization and analysis of crystal structures. *J. Appl. Crystallogr.* **2006**, *39*, 453–457. [[CrossRef](#)]